

SPICE-HL³: Single-Photon, Inertial, and Stereo Camera dataset for Exploration of High-Latitude Lunar Landscapes

David Rodríguez-Martínez^{1*}, Dave van der Meer², Junlin Song², Abishek Bera², C.J. Pérez-del-Pulgar¹, and Miguel Angel Olivares-Mendez²

Abstract

Exploring high-latitude lunar regions presents an extremely challenging visual environment for robots. The low sunlight elevation angle and minimal light scattering result in a visual field dominated by a high dynamic range featuring long, dynamic shadows. Reproducing these conditions on Earth requires sophisticated simulators and specialized facilities. We introduce a unique dataset recorded at the LunaLab from the SnT - University of Luxembourg, an indoor test facility designed to replicate the optical characteristics of multiple lunar latitudes. Our dataset includes images, inertial measurements, and wheel odometry data from robots navigating seven distinct trajectories under multiple illumination scenarios, simulating high-latitude lunar conditions from dawn to night time with and without the aid of headlights, resulting in 88 distinct sequences containing a total of 1.3M images. Data was captured using a stereo RGB-inertial sensor, a monocular monochrome camera, and for the first time, a novel single-photon avalanche diode (SPAD) camera. We recorded both static and dynamic image sequences, with robots navigating at slow (5 cm/s) and fast (50 cm/s) speeds. All data is calibrated, synchronized, and timestamped, providing a valuable resource for validating perception tasks from vision-based autonomous navigation to scientific imaging for future lunar missions targeting high-latitude regions or those intended for robots operating across perceptually degraded environments. The dataset can be downloaded from <https://zenodo.org/records/13970078?preview=1>, and a visual overview is available at https://youtu.be/d7sPeO50_2I. All supplementary material can be found at <https://github.com/spaceuma/spice-hl3>.

Keywords

planetary exploration, mobile robots, lunar navigation, perceptually degraded environment, SPAD, single-photon, visual odometry, SLAM, high-latitude, south-pole, PSR.

1 Introduction

Opportunities to acquire in-situ data to inform planetary exploration missions are often limited, an issue exacerbated when dealing with hardly accessible locations. A great number of missions currently aim at the lunar South Pole due to its expected abundance of resources and its potential to address key questions about the Moon’s origin and evolution (Padma 2023; Kleinhenz et al. 2024; Wang et al. 2024a). However, high-latitude lunar regions pose significant challenges for robotic and perception systems. The lunar South Pole, in particular, not only presents one of the most perceptually challenging environments any planetary rover has ever faced but also features some of the Moon’s most extreme terrain elevation changes. The small lunar obliquity to the ecliptic (of just 1.54°) produces very low solar elevation angles (often $<10^\circ$ (Zhang et al. 2023)), which, combined with the rugged terrain, results in a visual field dominated by dim lights and long, dynamic shadows. These shadows sweep across a monochromatic, and at times featureless, environment where negligible light scattering leads to an extremely high dynamic range (HDR) between the bright highland regolith and the darkness of crater floors and permanently shadowed areas.

Robots must, therefore, move fast in this environment—faster than ever before (Rodríguez-Martínez et al. 2019)—to avoid getting stranded in the moving shadows or succumbing to the freezing temperatures in permanent cold traps. Regardless of their level of automation, onboard perception systems must be capable of effectively resolving landmarks and other surrounding features with a high enough signal-to-noise to inform subsequent actions, even in darkness. As a result, successful navigation and scientific characterization in high-latitude lunar regions requires high frame rates, rapid exposure adaptations, and HDR imaging capabilities, which

¹Space Robotics Lab, Department of Systems Engineering and Automation, University of Malaga, Spain.

²Space Robotics Research Group, Interdisciplinary Research Center for Security, Reliability, and Trust (SnT), University of Luxembourg, Luxembourg.

* This work was partly conducted when the author was still affiliated with the Advanced Quantum Architecture Laboratory (AQUA), EPFL, Switzerland.

Corresponding author:

David Rodríguez-Martínez, Space Robotics Lab, University of Malaga, 29070 Malaga, Spain.

Email: david.rm@uma.es

may demand the use of innovative sensing technologies and approaches.

In this dataset, we present proprio- and exteroceptive data recorded with multiple fictionlab’s Leo rovers at the LunaLab of the Space Robotics Group at the SnT - University of Luxembourg (Ludvig et al. 2020). This dataset is unique in two ways. First, we make public the most exhaustive real lunar-like robotic onboard data to date, collected through a series of trajectories designed to mimic the negotiation of obstacles and navigation patterns of a rover traversing across high-latitude lunar regions. Visual data contained most perceptual artifacts expected from these missions, namely harsh and dynamic shadows, lens flares, motion blur, accumulated dust, poissonian noise, and HDR resulting in over- and undersaturated pixel values. Second, and for the first time, it includes data recorded using a novel Single-Photon Avalanche Diode (SPAD) camera. As we will discuss in Section 3.1, SPAD cameras represent a new sensing paradigm for vision-based robotic systems, making SPADs promising candidates as primary sensing instruments for exploring perceptually degraded environments like the lunar poles. The acquired data can be used to test and validate vision-driven tasks from navigation approaches to sensor processing algorithms.

1.1 Related datasets

Devising and testing new algorithms for vision-driven tasks require empirical data from higher lunar latitudes, which is currently lacking. Due to the limited access to the lunar surface, simulations are often the most cost-efficient solution. Several simulators have been developed in an attempt to synthetically replicate general features of the lunar environment (Pessia et al. 2019) or specific visual characteristics of the lunar poles (Richard et al. 2024; Fong 2024), but designing a fully representative digital lunar landscape while also synthetically producing accurate sensory data is a significant challenge. While synthetic datasets offer a valuable resource for simulating a broad range of visual scenarios, they are inherently limited in fully capturing the complex interplay of photometric, material, and sensor characteristics that occur in real lunar-like environments. The subtle variabilities and interdependencies that often arise in real-world environments—e.g., the effect of the lunar albedo and the way light is scattered through discrete surfaces like lunar regolith, with its varying grain sizes and composition—are challenging to accurately and efficiently model in synthetic environments, particularly when intended for large-scale robotic simulations.

The RCLLD dataset (Wang et al. 2024b) contains images acquired by the Chang’e-3, Chang’e-4, and Chang’e-5 lunar landers as well as panoramic images captured by the Yutu-1 and Yutu-2 lunar rovers. This might be considered one of the best labeled datasets ever captured of the lunar environment due to the true in-situ nature of the images and the varying lighting conditions and real visual artifacts it features, both from near and far side regions. The dataset presents, however, independent static frames without ground truth measurements, which, alongside the lack of sequential images, precludes its use for navigation-related algorithmic testing and evaluations.

In contrast, multiple published datasets attempt to recreate the unstructured and extreme nature of planetary environments through data recorded in analog Mars- and lunar-like regions on Earth. These include the Devon Island dataset (Furgale et al. 2012) recorded in the Canadian High Arctic, the LRNT (Vayugundla et al. 2018) and S3LI (Giubilato et al. 2022) datasets captured at Mount Etna by the German Aerospace Center (DLR), or the BASEPROD dataset (Gerdes et al. 2024) recorded in the natural badlands of Bardenas Reales, in northern Spain. While these datasets closely approximate some of the most challenging conditions expected during exploration missions, while presenting ground truth measurements and annotated data to greatly benefit the broader research community, they do not contain the lighting variations and harsh perceptual conditions characteristic of high-latitude lunar missions. This is the gap that we strove to bridge with SPICE-HL³.

Only a few analog facilities in the world are capable of recreating the complex photometric conditions of the lunar environment. To our knowledge, only two publicly available datasets exist to date aiming at replicating the expected visual features of high-latitude lunar regions. Both datasets were developed by the Intelligent Robotics Group at NASA Ames Research Center. The POLAR Stereo (Wong et al. 2017) and the POLAR Traverse (Hansen et al. 2024) datasets present a library of static stereo images from an analog lunar environment. The environment consists of a test bed filled with a soil simulant with albedo characteristics typical of actual lunar regolith (JSC-1A was used for the Stereo dataset, while a modified version of LHS-1 was used for the Traverse dataset). The scene also features rocks and craters and is illuminated by a 1kW tungsten-halogen light positioned to recreate the low solar elevation angles at the poles. The POLAR Stereo dataset presents a static viewpoint of a wide range of landscape configurations. In contrast, the POLAR Traverse dataset simulates motion through sequences of stereo images captured by moving the camera rig across a longer test bed. Both datasets include sub-centimeter LiDAR scans of the terrain and radiometric calibration data.

Despite the rigorousness in mimicking the photometric conditions expected in high-latitude lunar regions, both POLAR datasets have several limitations—particularly when used for vision-based data processing and robotic navigation research—which we have attempted to overcome with SPICE-HL³. The most significant issue is the static nature of the recording. Acquiring static images could be representative of some planetary navigational approaches in which the rover must stop, acquire images, map, and localize itself before moving again. But it limits the utility of the dataset for scenarios requiring higher duty cycles or continuous movement (e.g., localization while driving pipelines), preventing motion-related artifacts from affecting the images. In contrast, our dataset presents both static and dynamic image sequences, the latter captured at two different traversing speeds (5 and 50 cm/s). Additionally, the POLAR Traverse dataset presents stereo pairs captured at 1-meter intervals, resulting in a limited overlap between consecutive frames, which, in our experience, hampers feature tracking, especially under such harsh illumination conditions. Trajectories are also restricted to straightforward and backward motion. In our case, multiple compound

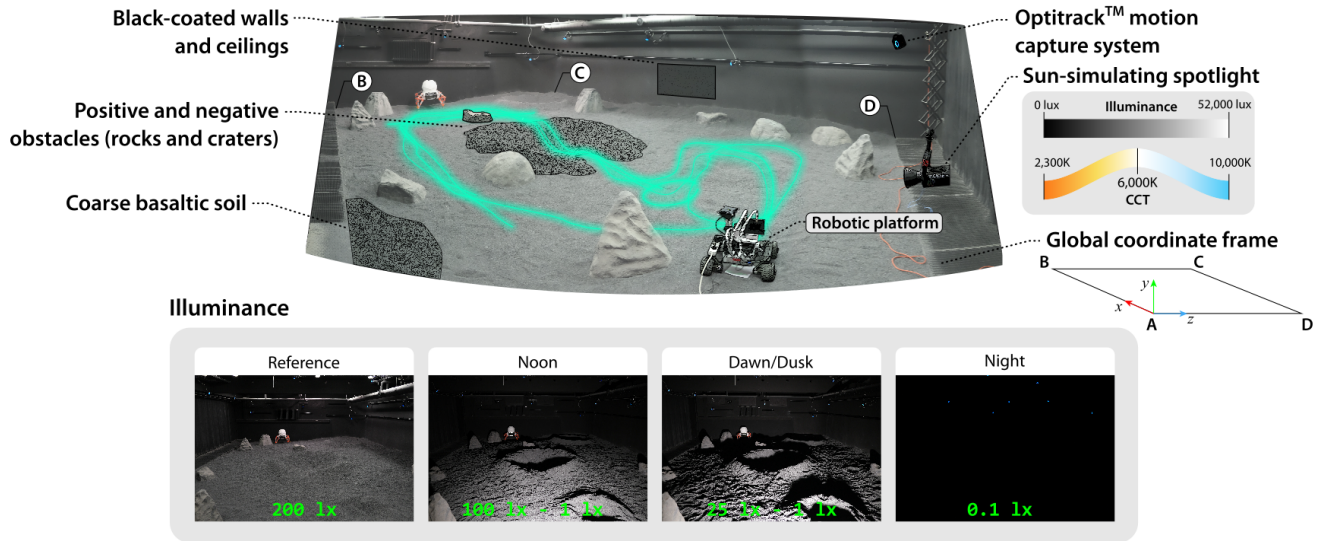


Figure 1. The LunaLab facility at the University of Luxembourg is designed to simulate lunar photometric conditions across multiple latitudes. This dataset contains images captured under four different illumination conditions, namely: reference, noon, dawn/dusk, and nighttime. Illuminance values were measured with a luxemeter located in bright and shaded areas across the center of the test field. The origin of the global coordinate frame is located at the camera position from where the top image was taken ('A'); the other 3 vertices of the global plane are also denoted in the image ('B', 'C', and 'D'). A visual reference of all the trajectories followed is overlaid in the image.

trajectories containing both forward motion and spot turns were recorded at high frame rates, with the spotlight affecting the field of view from multiple positions. Last, the presence of visible background elements, such as surrounding walls and equipment, in some of the images partially reduces NASA's datasets' fidelity, an issue that we attempted to overcome by eliminating most background elements and narrowing the cameras' lookahead distances.

2 Testing facility

The LunaLab consists of an $11 \times 8 \text{ m}^2$ lunar analog terrain designed to mimic the optical conditions found across different lunar latitudes (see Fig. 1). The facility is equipped with an Aputure's 600W LightStorm 600c Pro spotlight, whose vertical and horizontal position along the shorter side of the test bed, its color temperature (2,300 K–10,000 K), and its luminance (69 lux–51,100 lux) can be fully adjusted to simulated different sunlight elevation angles and daytime conditions. We recorded data under four different illumination conditions (Reference, Noon, Dawn/Dusk, and Night), as illustrated in Fig. 1. Noon and Dawn/Dusk conditions were obtained by positioning the spotlight at a height of 80 cm and 40 cm, respectively; simulating the low range of Sun elevation angles expected across a full lunar day at the poles (8° and 4° , respectively, with respect to the center of the test bed). For all the trajectories, we used a CCT of 6000 K to simulate sunlight color temperature in space. The testbed is filled with 20 tons of coarse basaltic gravel and features rocks and craters of varying sizes and shapes, which introduce additional shadows and occlusions. Black-coated walls and ceilings surround the test bed to minimize secondary light reflections, simulating the absence of a scattering atmosphere. Ground truth is acquired through 12 OptiTrack™ Prime^x motion capture cameras with sub-millimeter accuracy.

3 Sensor setup

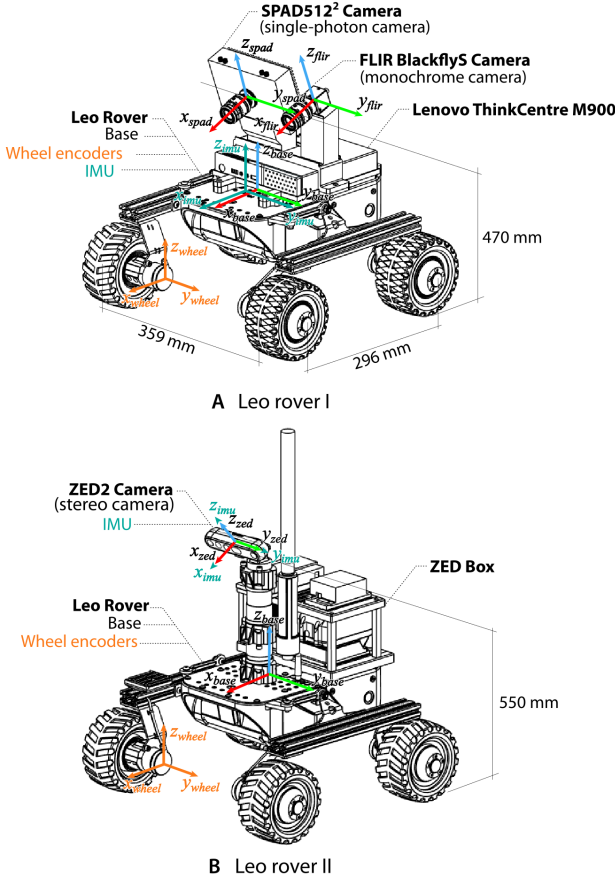
Our dataset was recorded using a variety of passive optics, including a monochromatic camera (Teledyne FLIR BlackflyS), a stereo-inertial sensor (StereoLabs ZED2), and a single-photon camera (PiImaging SPAD512²) (refer to Section 3.1 for additional details on single-photon imaging). The specifications of each of the cameras used are listed in Table 1. Inertial measurements were recorded either through the built-in Inertial Measurement Unit (IMU) on the Leo rover or the one on the ZED2. Additionally, odometric data was measured through in-wheel 12-PPR incremental rotary encoders.

The sensors used for data recording were mounted on two fictionlab's Leo rovers, each with a different sensor configuration. One rover incorporated the FLIR BlackflyS and the SPAD camera, while the ZED2 stereo camera rig was mounted on a second rover. Both rovers are powered by 4 Bühler DC motors controlled by a Raspberry Pi 4B. During data acquisition, the rovers were teleoperated via ROS2 from outside the lab over a 2.4 GHz Wifi network. Data for the FLIR and SPAD cameras were recorded on a separate Lenovo ThinkCentre M900 PC, while the stereo camera and IMU data were recorded directly on the rover's onboard computer. The FLIR and SPAD cameras were positioned approximately 470 mm from the ground and their mounts were designed to maintain a constant 20° pitch, resulting in a look-ahead distance of 0.5–10 m, which allowed the cameras to resolve immediate obstacles as well as part of the horizon while avoiding most of the surrounding background elements. In the case of the ZED2 camera, the mount was positioned 550 mm from the ground and at a 25° pitch incline. Figure 2 illustrates each rover configuration and sensor layout. The rovers also incorporated a headlight, which was used to record variations of illuminance during one of

Table 1. Camera sensors used and their specifications

	FLIR BlackflyS	StereoLabs ZED2	Pi Imaging SPAD512 ²
Camera type	Standard monochromatic	Stereo RGB	Single-photon
Sensor size	6.23×4.98 mm (1/2.9")	4.8×3.6 mm (1/3")	9.5×9.5 mm
Resolution	720×540	640×360	512×512
Pixel Pitch	6.9 μm	2 μm	16.38 μm
Bit Depth (raw)	8-bit	8-bit	1-bit
Effective Focal Length	14.24 mm f1.4	2.12 mm f2.0	14.88 mm f1.4
Field of View	21.6°×12.3°	100°×70°	35.5°×35.5°
Baseline	n/a	120 mm	n/a

the trajectories (see Section 4.3 for details on the different trajectories).

**Figure 2.** Robot configuration and sensor layout for both Leo rovers used during the recording of this dataset.

3.1 SPAD Camera

In this dataset, and for the first time, we present data recorded with a Single-Photon Avalanche Diode (SPAD) camera. SPADs are a novel set of imaging devices capable of detecting the arrival of individual photons between sub-10 picosecond time intervals, with wide dynamic ranges (>100 dB), and exceptionally low noise (Morimoto et al. 2020; Gramuglia et al. 2022). Single-photon resolution and minimal dead times are possible thanks to the use of Geiger-mode avalanche photodiodes and active quenching. Unlike conventional cameras, which provide a digitized signal equivalent to the amount of light intensity accumulated over time (0–255 per pixel, for 8-bit images), a SPAD pixel provides a direct binary output (0: no photon detected,

1: photon detected). Their extremely light-sensitive pixels, paired with fast data acquisition and their versatile data processing capabilities, make SPAD cameras a promising sensing technology for a wide range of applications, particularly those dealing with visually challenging scenarios where conventional cameras struggle to achieve enough signal-to-noise. SPADs have been primarily used in passive mode for biomedical imaging applications (Michalet et al. 2022) or in active mode, when combined with a synchronized light source, for time-of-flight (ToF) and Light Detection and Ranging (LiDAR) applications (Zhao et al. 2022).

In our case, we used the SPAD512² model from Pi Imaging Technologies as a passive camera to record monochromatic images meant to assist, for the first time, in visual-based scientific imaging and autonomous navigation pipelines. This camera has a resolution of 512×512, and it is capable of acquiring up to 100,000 binary frames per second (i.e., 1-bit images) with a minimum exposure time of 20 ns per frame. These binary frames could be later integrated to digitize images at higher bit depths. Figure 3 illustrates examples of the raw binary frames output by the SPAD and their equivalent higher bit-depth integration. As will be detailed in Section 4.1, we have developed a series of scripts that facilitates the programmatic acquisition of binary frames from the SPAD512² for robotic applications (i.e., acquisition of a predefined batch of binary frames at a given batch rate, which is not provided natively by the camera firmware) and the subsequent frame integration, which are provided in the **Supplementary Material** of this dataset.

4 Dataset

The dataset includes measurements from 88 distinct sequences recorded along seven different trajectories (A–G). Each trajectory presents multiple time-synchronized monocular and stereo image sequences, inertial measurements, and wheel odometry data captured under different illumination conditions, with variations in the type of movements performed, the speed of the rover, and/or the type of cameras used. We intended to record as many variations in movement and illuminance as possible to replicate the set of expected operational conditions during actual exploration missions to the lunar poles, resulting in a total of 1,289,958 images. The characteristics of each of the trajectories are listed in Table 2, and further details are provided in Section 4.3. The ground truth position of the rover with sub-millimeter accuracy is provided for every sequence. The layout of the test field and the rovers’ configuration remain invariant throughout the data collection campaign. The ground was raked after each

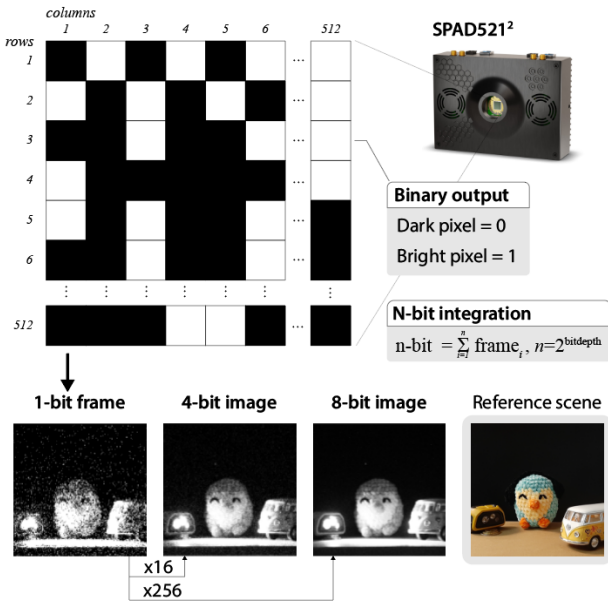


Figure 3. The SPAD512² camera acquires raw binary frames, which are a set of 1-bit-per-pixel frames that could be later integrated to form tailored bit-depth images.

run to prevent footprints from creating unnatural features on the terrain.

4.1 Data format

Image files from the SPAD512² and ZED2 cameras are provided in lossless PNG format, while images captured by the FLIR BlackflyS during *trajectory A* were recorded as JPG. The images captured by the FLIR and ZED2 cameras are stored in 8-bit format. While the FLIR frame rate varied with the preset exposure, the ZED2 stereo image sequences were acquired at 30 Hz. Disparity maps generated from the stereo images have been computed using Stereo Block Matching (SBM) and saved as 8-bit color-coded PNG files. The associated Python script is provided as part of the [Supplementary Material](#).

In the case of the SPAD camera, we offer different formats based on the type of trajectory. For the static trajectory (*trajectory A*), we provide sequences of raw binary frames (i.e., 1-bit format). In contrast, the dynamic trajectories include image sequences in a 4-bit format. This choice was due to memory constraints of the SPAD512², which limits continuous 1-bit-mode data acquisitions to a maximum of 130,000 frames. Given the exposure time used for dynamic sequences (typically between 0.5 μs–25 μs per binary frame), this constraint would have restricted the total recording time per trajectory to less than 3 s. Even though the exposure time could be manually adjusted, another limitation of the single-photon camera was its lack of built-in support for acquiring data at a given frame rate. To overcome these limitations, we wrote a series of custom scripts that allowed us to programmatically command the SPAD512² to capture an 8-bit-equivalent number of frames (256 in 1-bit mode, 16 in 4-bit mode) at a predefined frame rate (e.g., every 20 ms). Despite this improvement, we encountered a bottleneck during image acquisition in 1-bit mode that might be associated with network constraints or internal camera

limitations. It took on average 100 ms for the SPAD camera to process each batch of 256 binary frames regardless of the exposure time, effectively limiting the frame rate in 1-bit mode to about 10 Hz. For this reason, we opted for continuous 4-bit mode acquisition in the case of dynamic motion sequences. All the associated scripts are included in the utilities accompanying this dataset. We also provide each camera metadata—including *frame ID*, *timestamp*, *height*, *width*, and *file encoding*—organized into corresponding CSV text files. Example images from all the cameras and the different SPAD formats are illustrated in Figure 4.

We also include wheel odometry, IMU, and ground truth data, all formatted as CSV text files to ease readability. Wheel odometry and inertial measurements are provided relative to the frames of reference depicted in Figure 2.

Wheel odometry data consists of timestamps, computed linear and angular velocities, as well as the estimated 3-dimensional position derived from the averaged readings of every in-wheel encoder. Wheel odometry data were recorded at 20 Hz, with values expressed in meters and radians.

IMU data include timestamps, the rover’s orientation—expressed as a unit quaternion (x, y, z, w) with w as the scalar component—, the angular velocity and linear acceleration cartesian vectors, and their associated covariance values. Inertial measurements were recorded at 100 Hz, with values expressed in millimeters and radians.

Ground truth measurements are provided with respect to a global frame whose origin is defined according to Figure 1. Note that in this global frame, the negative y-axis corresponds to the gravity-aligned vector. Ground truth data includes timestamps, the rover’s 3-dimensional position, and its orientation—formatted in the same quaternion representation as the inertial measurements. Ground truth was recorded at 30 Hz, with values expressed in meters.

Alongside raw data, we provide recorded rosbags for every trajectory in an MCAP format*.

4.2 Data synchronization

Data was recorded on multiple dedicated computers and at different frame rates depending on the data source. To ensure accurate timestamping and synchronization across the computers, we established an internal network run by a Network-Time Protocol (NTP) server. This configuration allowed all the commanding computers to synchronize their clocks with millisecond accuracy. Timestamps are formatted in seconds since January 1, 1970, 00:00:00 (UTC), expressed with nanosecond-level precision; e.g., 1726152291.870697076.

4.3 List of trajectories

The recorded trajectories can be divided into 3 main groups. All the trajectories include wheel odometry, inertial, and ground truth measurements. Details of each trajectory are listed in Table 2, while the ground truth trajectories are depicted in Figure 4E.

Trajectory A consists of a long, compound path formed by 100 waypoints, covering a significant portion of the test field. Waypoints are spaced roughly 25 cm

*<https://mcap.dev/>

Table 2. Description of each trajectory recorded as part of the SPICE-HL³ dataset, its different visual conditions, and its associated data. “Seq.” indicates the number of distinct sequences per trajectory. Length for trajectories B–E is computed as the average among the different slow and fast runs.

Trajectories	Seq.	Description	Imaging Mode	Illumination Mode	Rover Speed	Cameras	Headlights	Length	Duration
Trajectory A	70	Compound static	Static	All	n/a	SPAD & FLIR	On/Off	4.37m	82831s
Trajectory B	4	Parallel to light source	Dynamic	Dawn/Dusk	Slow & Fast	SPAD & ZED2	Off	2.42m	55s / 19s
Trajectory C	4	Toward light source	Dynamic	Dawn/Dusk	Slow & Fast	SPAD & ZED2	Off	2.57m	58s / 13s
Trajectory D	4	Away from light source	Dynamic	Dawn/Dusk	Slow & Fast	SPAD & ZED2	Off	2.86m	52s / 17s
Trajectory E	4	Spot turns	Dynamic	Dawn/Dusk	Slow & Fast	SPAD & ZED2	Off	0.53m	58s / 15s
Trajectory F	1	Compound dynamic	Dynamic	Dawn/Dusk	Slow	ZED2	Off	11.51m	309s
Trajectory G	1	Compound closed-loop	Dynamic	Dawn/Dusk	Slow	ZED2	Off	12.18m	265s

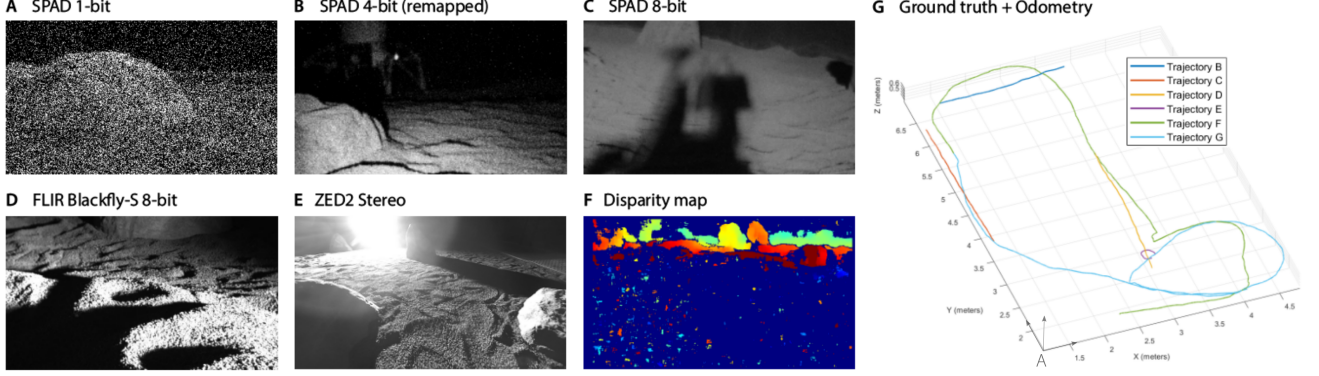


Figure 4. Examples of the different images, formatting, and odometric measurements provided in the SPICE-HL³ dataset. Images are cropped to a 16:9 ratio in this figure for illustration purposes only.

apart to ensure sufficient overlap between consecutive frames. At each waypoint, the rover halts to capture static images and record measurements, mimicking the operational behavior of most planetary rovers. Taking advantage of the stationary nature of this trajectory, we tested seven different illumination conditions at each waypoint (i.e., Reference, Noon, Dusk/Dawn, and Night, as defined in Section 2), with the last three conditions both with and without the rover’s headlights switched on. For each lighting scenario, images are taken at five different exposure times. During this trajectory, only monocular images were captured using the FLIR Blackfly-S and the SPAD512² cameras. For the SPAD camera, 256 binary frames (1-bit format) were recorded for each exposure time.

Trajectories B–E involve short movements, ranging from 12.5 to 62 s, during which images are continuously acquired. Each trajectory represents a different driving direction relative to the Sun-simulating spotlight (see details in Table 2). For all these trajectories, the illumination scenario is set to Dawn/Dusk with the rover’s headlights turned off. Images were captured using both the ZED2 stereo camera and the SPAD512² camera. For the SPAD512², single-photon frames were saved in a 4-bit format with fixed equivalent exposure times as follows:

- Trajectory B: 400 μ s per frame at 215–510 Hz
- Trajectory C: 135 μ s per frame at 120–440 Hz
- Trajectory D: 100 μ s per frame at 125–154 Hz
- Trajectory E: 150 μ s per frame at 30–120 Hz

These exposure times were chosen based on the recommended settings from the SPAD built-in autoexposure module. Note that for the SPAD512², exposures must be preset before image acquisition. The associated frame rates correspond to the slow and fast motion recording,

respectively. The dataset includes raw 4-bit images. However, a script to remap these images into an 8-bit colormap for visualization purposes has been included in the **Supplementary Material**. In contrast, the ZED2 camera was operated in autoexposure mode, and we provide both left and right 8-bit rectified monochromatic images. Image sequences from both cameras were recorded at two different rover speeds: slow (5 cm/s and 0.1 rad/s) and fast (50 cm/s and 1 rad/s).

Trajectories F–G consist of continuous, compound paths where stereo images are continuously acquired using only the ZED2 camera. The rover moves across the test field for a distance similar to that of the static *trajectory A*, but this time combining different segments of motion without stopping at each step. *Trajectory G* forms a loop by revisiting some of the locations previously traversed during *trajectory F*. We chose to separate these into two distinct trajectories due to a significant gap in the timestamps between them. However, users of the dataset have the option to treat both trajectories as a single sequence by merging the imaging data.

4.4 Data structure

Data files are provided in individual ZIP files including every sequence for each of the recorded trajectories. These ZIP files are structured as illustrated in Figure 5. Every image file follows the same naming convention, i.e., ‘cameratypetimestamp_frameID.*’.

4.5 Supplementary material

We provide the following Python and Matlab scripts to supplement this dataset. The script files are provided alongside the dataset, but we encourage readers to find the latest versions at <https://github.com/spaceuma/>

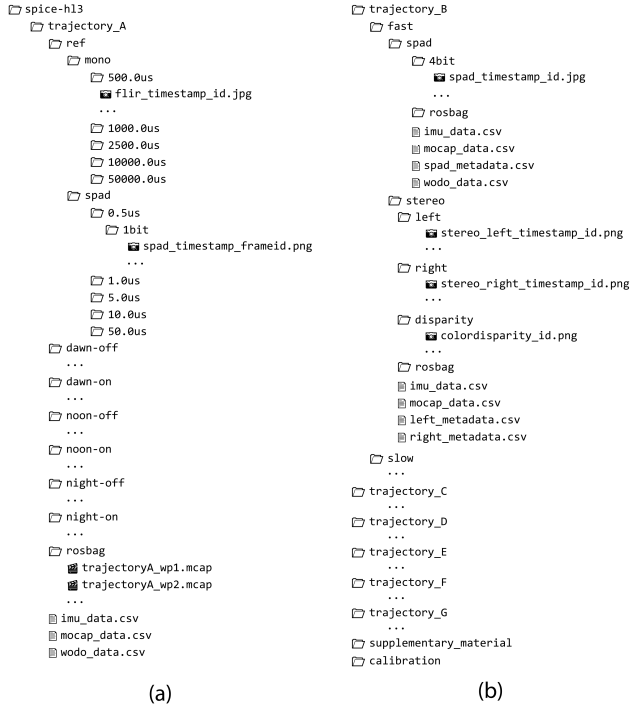


Figure 5. Structure of the provided ZIP files storing all the trajectories and data file naming convention. Two types of directory structures can be found: a) directory tree corresponding to trajectory A and b) directory tree corresponding to trajectories B–G. For each type of directory, we illustrate an example structure of only one of the trajectories. The remaining trajectories listed for each type follow a similar structure.

spice-hl3. These scripts are designed to be easily adaptable to the ultimate end-user needs.

- `SPAD_1bit_capture.py` and `SPAD_1bit_cont.py` allow the user to capture a predefined number of binary frames or a continuous stream of binary frames at a given batch rate, respectively.
- `multiexposure_launcher_SPAD.bat` allows the user to call the former script to capture a number of binary frames at five different exposure times.
- `digitize_1bit2nbit.m` and `digitize_4bit2nbit.m` are meant to integrate multiple 1-bit and 4-bit raw files and export them into PNG images of a given bit depth. We provide the latest version of these and other scripts required to programmatically operate Pi Imaging’s SPAD512² camera in the associated repository[†].
- `disparity.py` computes disparity maps for multiple stereo image pairs and saves the output as PNG images.
- `remap.m` transforms 4-bit frames into normalized 8-bit equivalent colormap PNG images.

Additionally, we provide recorded rosbags for each trajectory in an MCAP format. Each rosbag includes ground truth data, wheel odometry and inertial measurements, and in those cases where the ZED2 stereo camera is used, both left and right images rectified RGB and monochrome images.

5 Sensor calibration

5.1 Intrinsic calibration

The dataset includes the intrinsic calibration parameters for each of the cameras used. This can be found within the `camera_intrinsics.json` file. Camera intrinsics have been estimated using a 2-coefficient calibration and the pinhole camera model, which include the focal lengths (f_x , f_y), the optical center (c_x , c_y), and the radial and tangential distortion parameters (k_1 , k_2 , p_1 , p_2). We provide the original set of images used for calibration in the event that the end-user of the dataset prefers a different method. Note that single-photon calibration images are provided in an 8-bit format.

5.2 Extrinsic calibration

To evaluate the localization accuracy of visual odometry and SLAM algorithms, the precise spatiotemporal relationship between cameras and ground truth measurements must be known. We implemented the target-based calibration approach described in Song et al. (2024). This method uses offline, full-batch nonlinear least squares optimization to determine camera calibration parameters, namely: ${}^C_M T$, which represents the rigid body transformation from the global frame, M , to the camera frame, C ; and t_d , which defines the time offset between the ground truth and camera clocks. Camera-to-global and camera-to-camera extrinsics, as well as all the transformation matrices from IMU and wheel encoders, are listed in the `sensor_extrinsics.json` file. We also provide the original set of calibration images used. Additionally, we provide the CAD model of each rover as part of the **Supplementary Material** of this dataset.

6 Evaluation

One of the key challenges in enabling autonomous robotic exploration of high-latitude lunar regions is the extreme and variable lighting conditions. With the Sun remaining low on the horizon, the terrain is characterized by deep, elongated shadows and intensely reflective sunlit areas due to the rugged topography and the absence of atmospheric scattering. These conditions can introduce numerous imaging artifacts, including oversaturation, flaring, and blooming when facing the Sun, or the apparent sectional brightening of the image when facing away from it (the so-called opposition effect). Such distortions can significantly impact the performance of downstream vision-based algorithms.

To ensure robust perception, exteroceptive sensors must be capable of adapting to these extreme and often rapidly varying illumination conditions.

To evaluate the utility of our dataset, we present a preliminary qualitative and quantitative evaluation of the imaging quality of the optical cameras used in this dataset as well as two potential use cases that, we believe, could spark innovative research in the domain of state estimation and

[†]<https://github.com/spaceuma/spice-hl3>

autonomous localization under GNSS-denied, perceptually degraded, unstructured environments.

6.1 Single-photon imaging

In the context of planetary exploration, accurate and reliable visual data is essential for scientific observations and contextualization, as well as for localization and mapping tasks during navigation. Published studies evaluating the passive imaging performance of large SPAD pixel arrays under perceptually degraded conditions remain limited. We, therefore, conducted a focused evaluation of the imaging quality of the SPAD512S camera under the range of illumination conditions presented in this dataset and compared its performance to the more commonly used stereo and monocular camera types. We assess each camera performance based on both qualitative and quantitative imaging quality metrics. We highlight differences in brightness, detail retention, and the presence of image artifacts, and include metrics such as dynamic range, histogram distribution, and PIQE (Perceptual Image Quality Evaluator)[‡]

Due to the wide variability in lighting conditions captured within our dataset, we focused this evaluation on the most visually challenging scenarios. As illustrated at the top of Figure 6, the single-photon sensitivity of the SPAD camera allows it to resolve image features with minimal undersaturation, far beyond the capabilities of the FLIR during dawn/dusk and nighttime drives. This is especially evident along the right-side edge of the rock located right in front of the rover. Under such conditions, SPAD frames present a higher dynamic range, lower PIQE score (note that PIQE is inversely correlated with perceptual quality) and a more uniform distribution of pixel intensities, particularly in the Dawn/Dusk scenario. Even during the nighttime drives, the SPAD captured 3.5 times greater pixel intensities than those recorded by the FLIR camera. It is worth noting that these metrics are achieved with the SPAD using half of the 8-bit-equivalent exposure time compared to the FLIR.

During sun-facing drives, the ZED2 camera achieved higher contrast and a wider distribution of pixel intensities, contributing to far better dynamic range than the SPAD. However, the ZED2 suffered from significant oversaturation, failing to capture scene details near the light source (see, e.g., the background rock in the upper-left corner of the image, only fully visible in the SPAD frame). Sun-facing drives represent one of the most challenging perceptual scenarios for vision-driven robots and autonomous vehicles due to the oversaturation and associated artifacts caused by direct sunlight and the limited ability of most cameras to simultaneously resolve both brightly lit and shadowed areas in a single shot. Thanks to their fast binary frame acquisition and nonlinear response to incident light, SPADs avoid the abrupt full-frame saturation observed in more traditional sensors, albeit with a lower contrast. The fast frame rate of the SPAD also mitigates image artifacts like lens flares, blooming, and smearing, otherwise visible in the ZED2 frames.

Overall, the SPAD appears to demonstrate a more uniform performance under extreme lighting, both low light and high-dynamic range, by preserving visual structure and detail where other cameras either saturate or fail to capture

usable data. Qualitatively speaking, the FLIR performed well overall but struggled with low light, needing longer exposure times at the risk of incurring in excessive motion blur when speed increases. The ZED2 excelled in contrast but suffered in high-dynamic-range conditions, which may pose challenges during dusk-to-dawn transitions or when directly facing the Sun.

While this analysis represents an important first step toward evaluating the sensing capabilities of various imaging modalities (single-photon binary vs traditional CMOS), it also underscores the limitations of commonly used quantitative imaging evaluation metrics. Metrics such as PIQE, while useful for approximating perceptual quality, are sensitive to scene texture and lighting variability, and thus may not fully reflect the operational performance of a given sensor across diverse conditions. Extracting conclusions from single frames using texture-based metrics can be misleading, particularly in environments with significant lighting variation, as those experienced in our lunar analog trajectories. At the bottom of Figure 6, we present the distribution of PIQE scores for each camera and illumination condition, computed over full trajectory sequences (i.e., 100 waypoints of trajectory A during dawn/dusk and night, and 5470 SPAD 8-bit frames alongside 535 ZED2 frames from the sun-facing trajectory C). For each case, the best- and worst-rated frames based on PIQE scores are displayed to provide qualitative context. Interestingly, despite the SPAD’s consistent ability to capture finer details and produce tighter, more stable PIQE distributions (clustered around the mean), both the FLIR and ZED2 cameras achieved lower absolute minimum and mean PIQE values. This can be attributed to several factors. The slightly higher resolution of the FLIR and ZED2 resulted in more texture-rich images under even lighting conditions, which can favor metrics like PIQE. Additionally, their narrower fields of view reduced the visibility of specular ground reflections—often intensified by artificial lighting such as headlights—commonly seen in SPAD images, and which may degrade perceptual quality scores.

Beyond resolution and field of view, a range of sensor-specific properties, such as pixel pitch, effective focal length, and even less frequently discussed factors like fill factor and quantum efficiency, significantly influence imaging performance and perceived quality. In this sense, novel technologies like the SPAD still have room for improvement compared to highly developed, conventional imaging technologies. These underlying physical characteristics not only shape image quality in specific scenarios but ultimately define the contexts and applications in which a sensing technology can be most effectively employed. As such, while perceptual quality metrics offer a helpful baseline, a comprehensive evaluation of sensor suitability for planetary exploration must account for the full imaging pipeline, mission-specific demands (particularly those concerning bandwidth and computational load), and

[‡]PIQE is a no-reference quality metric that estimates image distortion by analyzing local variance across non-overlapping 16×16 pixel blocks, providing an overall assessment of the percentage of low-quality or distorted blocks, i.e., those characterized by extreme saturation, low contrast, or pronounced blurring.

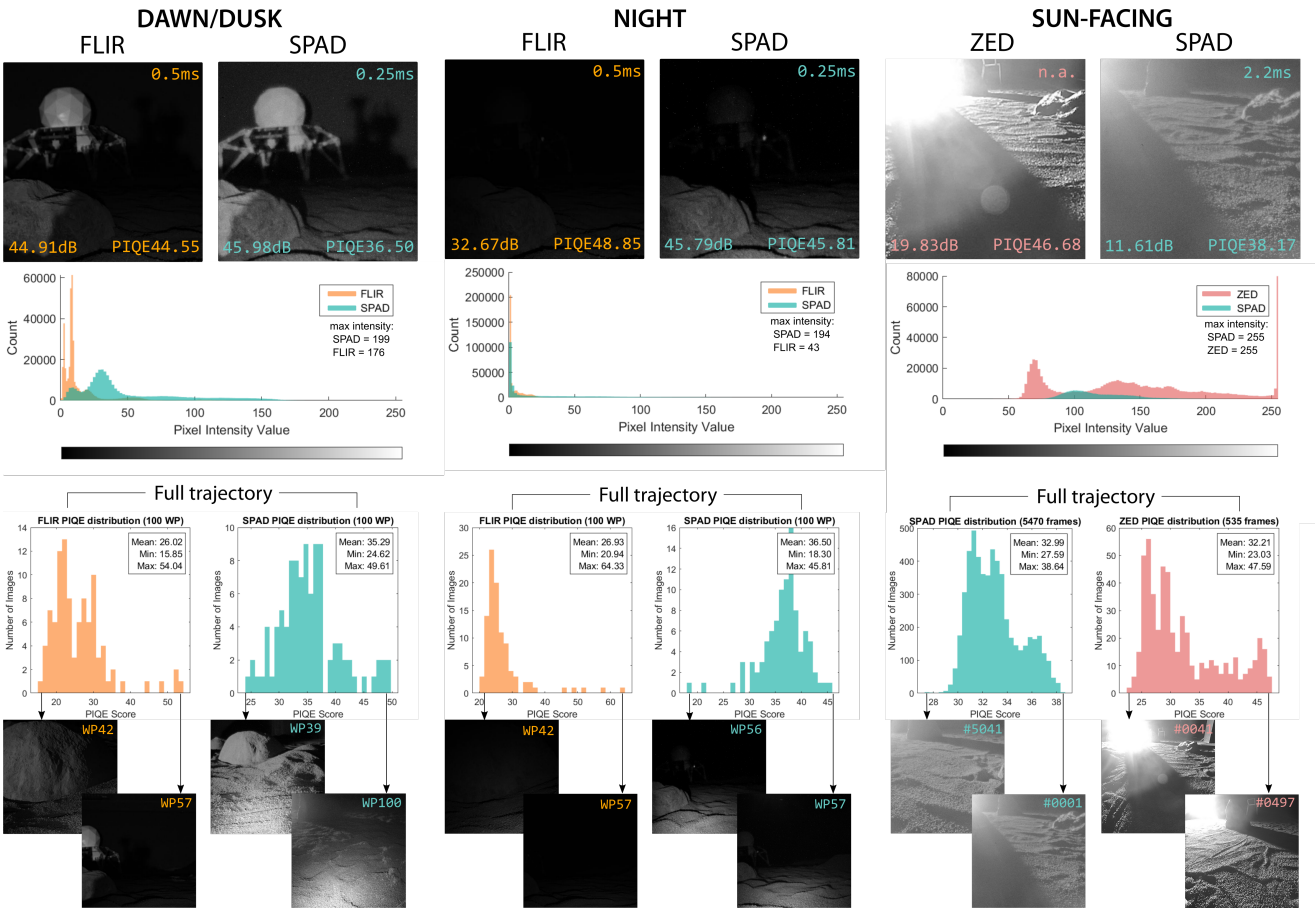


Figure 6. Performance evaluation of the FLIR, ZED, and SPAD cameras under extreme visual conditions. FLIR and ZED frames are cropped to match SPAD’s field of view. SPAD frames are digitized to 8-bit images. DAWN/DUSK and NIGHT frames belong to trajectory A with single frame captured at waypoint 58, while SUN-FACING frames belong to trajectory C with single frame captured as frame 10 in the sequence.

the complex interplay between hardware characteristics and environmental conditions.

Ultimately, these properties and metrics such as texture, contrast, field of view, dynamic range, and signal-to-noise, among others, may influence downstream vision-driven tasks in different ways. On their own, they are insufficient to determine the suitability of a sensor for a specific task. In the following sections, we used one of the captured SPAD images to conduct a preliminary analysis of the feature matching capabilities of lower bit-depth frames and the ZED2 stereo pairs recorded during the looped trajectory (F and G) to assess overall localization performance.

6.2 Feature matching with low-dimensional visual data

The use of SPAD cameras allows native access to image data with reduced pixel bit depths, which can significantly enhance computational efficiency, at least on paper. This potential improvement would be particularly valuable for resource-constrained applications, such as planetary robotic navigation, where extensive data pre- and postprocessing may be required. As a first step in evaluating this hypothesis, we benchmarked several widely used feature descriptors—namely, SIFT (Lowe 2004), SURF (Bay et al. 2006), and ORB (Rublee et al. 2011)—on two consecutive

image frames. We applied these algorithms to 2-bit, 4-bit, 6-bit, and a conventional 8-bit image format, which we derive from a 1-bit raw SPAD acquisition using our `ditigize_1bit2nbit.m` script. Features are then matched using a simple nearest neighbor search. We assess the performance of each algorithm across bit depths based on the number of detected keypoints, the ratio of RANSAC inliers (computed from the homographic transformation between images), and the relative execution time. A visual depiction of the results is illustrated in Figure 7, and the numerical results are listed in Table 3. To enable these algorithms to work with lower-bit-depth images, we remapped each image pair to an 8-bit-equivalent color map. Although these algorithms were designed to handle high-dimensional data, results indicate that lower-bit-depth formats can still yield a comparable number of keypoints and inliers. The restrictive value range in lower-bit images and the loss of intensity continuity when remapped, however, appear to pose challenges, resulting in significantly longer execution times. Limited intensity values could lead to a lack of distinctive features and increased noise and ambiguity in matching. Developing feature descriptors specifically optimized for lower bit-depth images could pave the way for new research avenues, particularly in the application of single-photon cameras in robotics.

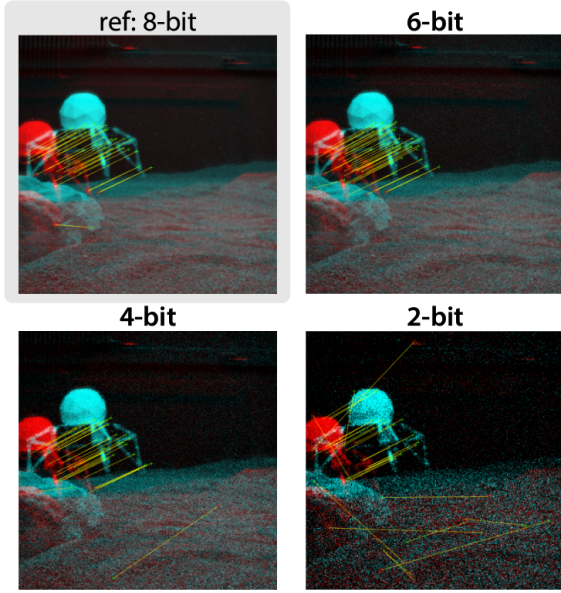


Figure 7. SURF-based feature matches between two consecutive images taken by the SPAD at different bit depths. Images belong to waypoints 57 and 58 of *trajectory A* under reference illumination conditions.

Table 3. Performance of different feature matching algorithms with varied n -bit image data.

Algorithm	Metric	2-bit	4-bit	6-bit	8-bit
SIFT	inlier %	n.a.	62	100	88
	keypoints	1	13	11	26
	rel. time	2.19	1.09	0.99	1.00
SURF	inlier %	23	53	68	74
	keypoints	31	32	40	34
	rel. time	6.51	2.34	2.33	1.00
ORB	inlier %	62	28	66	88
	keypoints	8	64	59	67
	rel. time	39.69	15.27	4.87	1.00

6.3 Stereo visual odometry

Another promising research direction aided by this dataset would be the study of visual odometry and SLAM pipelines in perceptually degraded scenarios. Conventional algorithms are often designed for optimal lighting conditions, where distinguishable features and minimal changes in brightness across frames are expected. However, when these algorithms are applied to images captured under extreme illumination conditions as presented in our dataset, they frequently fail to produce accurate pose estimates. Figure 8 illustrates the results of running wheel, inertial, and two well-known visual odometry pipelines—RTAB-Map (Labbe and Michaud 2019) and ORB-SLAM3 (Campos et al. 2021)—on images captured during the fast sequences of trajectories B–G. Trajectory A was deliberately excluded due to the significant variability in lighting conditions and camera exposure times explored within this trajectory. We also excluded SPAD camera data from this evaluation since its novelty, as characterized in the previous section, often requires customized adaptations to conventional odometry pipelines; adaptations that are beyond the scope of this work.

We have computed the accuracy of the different odometry methods based on the Absolute Trajectory Error (ATE).

In the case of ORB-SLAM3, we computed estimated trajectories based on both monocular and stereo camera configurations. All sequences evaluated are based on the ZED2 camera stream recorded with the Leo Rover II at fast speed (50 cm/s and 1 rad/s). Results are listed in Table 4. A visual representation of the accuracy of the estimated keyframe-based trajectories is shown in Figure 8. Default configuration parameters were used for RTAB-Map and ORB-SLAM3 methods.

Wheel odometry demonstrates relatively low error—comparable to vision-based estimations—in those scenarios where directional changes and slippage are minimal (e.g., Trajectory B and D), but its performance degrades in more complex scenarios. In contrast, pure inertial odometry consistently exhibits extremely high localization errors across all trajectories, significantly impacted by cumulative drift, even after applying initial low-pass filtering and static bias corrections. Visual-odometry methods, particularly ORB-SLAM3 in stereo mode, provide the most consistent and accurate performance overall. Notably, monocular ORB-SLAM3 underperforms relative to stereo variants, underscoring the value of depth perception for robust localization. While ORB-SLAM3 generally produced more accurate results, RTAB-Map demonstrated greater robustness in maintaining full-trajectory estimations under varying speed conditions. Somewhat unexpectedly, ORB-SLAM3 struggled particularly with slower-moving sequences, like F and G, frequently losing track and failing to relocalize, largely due to the open-loop nature of many of the trajectories. Insufficient motion between frames, especially in perceptually degraded scenes characterized by repetitive and indistinguishable textures (e.g., soil surfaces featured in our dataset), can result in low inter-frame disparity (parallax), leading to ambiguous feature associations. In contrast, faster motion introduces greater (but not excessive) spatial variation, which improves the reliability of feature-based approaches. These results suggest the existence of both lower and upper thresholds for frame-to-frame disparity, significantly influencing tracking performance, particularly in perceptually degraded environments.

As expected, however, vision-driven pipelines generally struggle with the visual complexity present in most of the recorded sequences, exhibiting moderate (approximately 5% of total distance traveled) to large localization errors (up to 60% of total distance traveled in those cases where tracking was not completely lost). Contributing factors include sparse and geometrically ambiguous scene features, strong, near-horizon lighting, long moving and occluding shadows, and repetitive or insufficient textures. Such conditions demand, on one hand, rapid adaptation capabilities from the sensing equipment (e.g., high dynamic range, fast exposure adaptation), and on the other, a carefully designed and fine-tuned data processing, localization, and mapping pipeline that exceeds the robustness of widely used SLAM frameworks.

Figure 8 also illustrates challenging frames representative of each trajectory, highlighting the types of visual conditions that future vision-based navigation systems for high-latitude lunar missions will need to overcome. Among all the trajectories tested, the one in which the rover moved away from the Sun exhibited the lowest performance, with tracking

lost in most cases, regardless of the localization approach used. Backlighting, particularly at low solar elevation angles, creates long and strong shadows that occlude most of the terrain right in front of the rover. This is especially relevant for small-sized exploration robots, which may feature limited fields of view and shallow lines of sight. Features along the edges of these self-generated shadows are often identified and tracked over time. Due to the dynamic morphology of these shadows as they adapt to terrain variations, the tracked features often result in pose estimation errors and reduced localization accuracy. Overall, these findings underscore the need for domain-specific odometry pipelines that can better accommodate the unique perceptual challenges of high-latitude lunar environments in order to enable accurate and reliable localization and mapping.

7 Known issues and challenges

During the development and processing of the SPICE-HL³ dataset, we encountered several challenges and limitations that should be highlighted for future users of the data. These issues primarily relate to the fidelity of the simulated lunar environment, the lighting conditions, and the synchronization of the different data sources.

7.1 Scene fidelity

True lunar regolith composition and grain size distribution affect how light reflects off the surface. Lunar regolith contains grains orders of magnitude smaller than the smallest grain of soil used in the LunaLab facility (lunar regolith contains grains of 40–130 μm (Carrier III 1973) compared to the 0.2–4-mm grains of the LunaLab soil). This mismatch affects the photometric characteristics of our images compared to those captured at facilities featuring advanced lunar regolith simulants meant to replicate lunar albedo to a higher degree of fidelity or those that will be eventually taken at the lunar poles. Some effects were irreproducible in the LunaLab, e.g., the opposition or halo-like effect caused by the coherent backscattering of light as it bounces off the crystalline minerals within the regolith grains when viewed from phase angles close to zero (i.e., backlighting). On the other side, while higher photometric accuracy would have been preferred, it would have also been extremely costly to do so. This is due to the size of the test bed and the safety measures required when operating with soils that include silty and clay particles. Nonetheless, the lower reflectivity of our soil compared to true regolith still serves us as a worst-case optical scenario.

In addition, the lighting setup within the LunaLab imperfectly replicates lunar sunlight conditions. Due to constraints related to the size of the test bed and the proximity of the light source, light decays inverse-squared within the length and width of the test bed. This leads to uneven illumination across the scene. Ideally, a perfectly collimated light source should be used so that illuminance remains uniform across the test bed, as it would be expected over relatively large distances on the Moon. Users of the data should expect slight inconsistencies in image exposure, particularly during the longer trajectories.

7.2 Data synchronization

The different computers commanding each of the cameras and the one logging ground truth data were not hardware-synchronized, which, given the millisecond-accuracy of our NTP network, could lead to compounded offsets between the timestamps of different data sources. We consider the impact of this drift to be negligible given the short duration of each of the trajectories, the speed of the rovers, and the high frame rates used.

We also observed slight mismatches between the left and right image streams of the stereo camera. This problem may have been caused by the lack of hardware-driven strict synchronization between the two camera streams, leading to discrepancies in frame timestamps and occasional frame drops. To ensure reliable stereo correspondence, we filtered the dataset to retain only matched frame pairs and discarded any frames with unmatched timestamps. The original unfiltered frames can be accessed by exporting the raw data from the *rosbags* provided for each trajectory.

7.3 Delayed ROS2 pipeline

During the recording of stereo camera data via ROS2, we observed that a subset of captured camera frames (approximately 8%) were assigned delayed timestamps relative to their capture sequence ID. We believe this issue might stem from the ROS2 image pipeline publication-time tagging, leading to occasional inconsistencies due to processing or queuing delays. As the frames themselves are sequentially numbered without loss, we addressed this by post-processing the data. Delayed timestamps are corrected and frames are renamed by interpolating expected capture times based on the average frame interval within each sequence. This ensures consistent temporal alignment required for downstream tasks.

Delays were also observed in the inertial measurements recorded. Although IMU was configured to operate at 200 Hz, an analysis of the data reveals that, after accounting for delayed and missing data packets, the effective sampling rate across all trajectories falls to approximately 50 Hz. This reduction in IMU data rate could compromise the performance of visual-inertial pipelines like ORB-SLAM3, as the lower frequency provides insufficient motion information between consecutive camera frames, reducing the accuracy and reliability of the IMU preintegration process. The combination of delayed camera frames and insufficient IMU measurements also leads to frequent instances where IMU measurements are either unavailable or inadequate for certain image frames, ultimately resulting in tracking failures and recurrent map resets as observed during our evaluation with ORB-SLAM3.

7.4 Coordinate transformations

The default coordinate frame for collecting the ground truth data is defined so that the negative y-axis corresponds to the gravity-aligned vector while the z-axis points toward the short side of the test field. This should be noted when comparing ground truth data with the motion estimated in either the optical frame or the robot frame.

The ZED2 stereo camera has a slight down tilt of 25°. On this rover, the ground truth tracker is mounted directly on

Table 4. Absolute Trajectory Error (ATE) reported as RMSE (maximum drift) in centimeters for wheel, inertial, monocular, and stereo sequence, evaluated over the fast (50 cm/s, 1 rad/s) motion profile. The symbol \times indicates unsuccessful trajectories where tracking was lost and could not be recovered. The best estimation for each trajectory is highlighted. Wheel odometry data for trajectories F and G was not recorded and, therefore, not included in the analysis.

Method	Trajectory B	Trajectory C	Trajectory D	Trajectory E	Trajectory F	Trajectory G
Wheel Odometry	34.66 (63.91)	124.87 (213.86)	85.40 (123.33)	\times	—	—
Inertial Odometry	473.97 (1183.15)	928.11 (2341.06)	816.84 (2384.15)	\times	\times	\times
ORB-SLAM3 Monocular (Campos et al. 2021)	100.27 (168.82)	94.04 (159.92)	\times	\times	\times	\times
RTAB-Map Stereo (Labbe and Michaud 2019)	64.77 (97.44)	\times	\times	29.12 (35.29)	64.50 (95.65)	145.56 (202.12)
ORB-SLAM3 Stereo (Campos et al. 2021)	83.72 (135.86)	83.23 (135.47)	\times	17.31 (31.72)	\times	\times

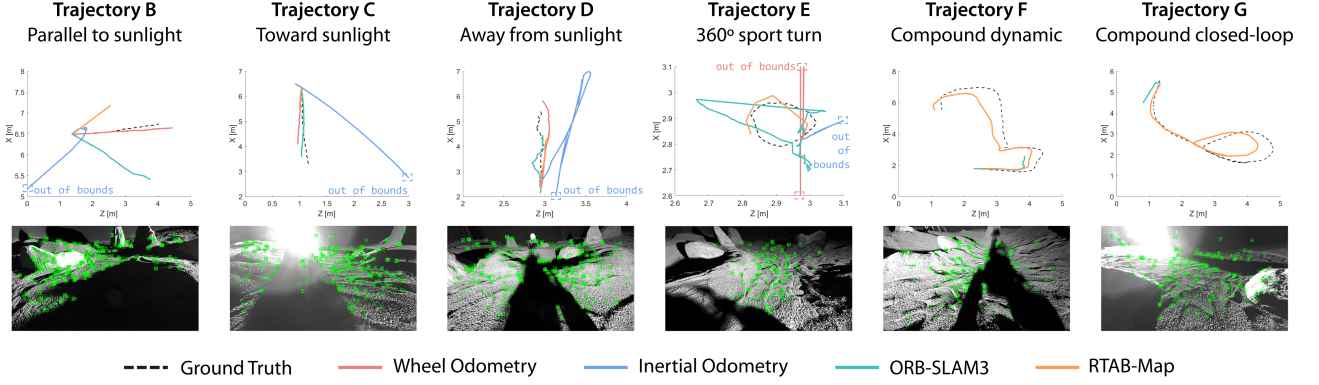


Figure 8. Best estimated trajectories obtained for wheel, inertial, RTAB-Map, and ORB-SLAM3 stereo methods; see Table 4 for quantitative results. For each trajectory, a representative critical frame is shown below the plot, corresponding either to the point of maximum absolute trajectory error (ATE) or to the point preceding a localization failure.

top of the stereo camera rig and, therefore, is affected by this same pitch angle. In contrast, on the rover carrying the SPAD and FLIR cameras, the ground truth tracker is mounted flat on a separate mast behind the camera mounts.

7.5 Effect of secondary light sources

Despite our efforts to recreate the low-scatter, high-contrast lighting conditions characteristic of lunar environments, we overlooked the impact of the motion capture system itself in artificially illuminating the scene. Specifically, the dim status LED rings on the motion capture cameras and the IR light they emit to track reflective markers on the rover inadvertently became secondary light sources. This is primarily noticeable under the most light-deprived conditions, such as during dusk/dawn and nighttime drive sequences without the use of headlights.

The faint visible light from the status LED rings is most apparent, despite affecting all cameras equally, in the longer-exposure images captured by the FLIR camera. This issue could have been mitigated by disabling or covering the status LED of all cameras. However, they served a useful purpose in identifying and troubleshooting motion capture camera issues during testing.

More significantly, the IR illumination used by the motion capture system for tracking the rovers introduced an unavoidable effect due to the partial sensitivity of most camera sensors to near-infrared light. This led to faint glows, ghosting, and occasional lens flares. These effects are evident in some of the ultra-fast binary frames captured by the SPAD. While these artifacts are likely present across all cameras, their prominence depends heavily on sensor characteristics and exposure times.

Acknowledging the presence of these effects is important for correctly interpreting the dataset and guiding future sensor deployments under similar experimental setups. Future data collection will incorporate strategies to better isolate imaging sensors from unintended secondary light sources to further improve the fidelity of simulating lunar photometry.

Dataset Website

The dataset can be found at <https://zenodo.org/records/13970078?preview=1>. The dataset is currently in restricted mode and can only be previewed. Data will be released at the time of publication of this paper. A quick visual overview of the dataset can be watched at https://youtu.be/d7sPeO50_2I. All supplementary material can be found at <https://github.com/spaceuma/spice-hl3>.

References

- Bay H, Tuytelaars T and Van Gool L (2006) SURF: Speeded up robust features. In: *Computer Vision—ECCV 2006: 9th European Conference on Computer Vision, Graz, Austria, May 7–13, 2006. Proceedings, Part I* 9. Springer, pp. 404–417.
- Campos C, Elvira R, Rodríguez JJG, Montiel JM and Tardós JD (2021) Orb-slam3: An accurate open-source library for visual, visual-inertial, and multimap slam. *IEEE transactions on robotics* 37(6): 1874–1890.
- Carrier III WD (1973) Lunar soil grain size distribution. *The moon* 6(3): 250–263.
- Fong T (2024) Digital Proving Ground: VIPER rover simulator (RSIM). In: *2024 Lunar Surface Innovation Consortium (LSIC) Fall Meeting*. LSIC.

- Furgale P, Carle P, Enright J and Barfoot TD (2012) The devon island rover navigation dataset. *The International Journal of Robotics Research* 31(6): 707–713. DOI:10.1177/0278364911433135.
- Gerdes L, Wiese T, Castilla Arquillo R, Bielenberg L, Azkarate M, Leblond H, Wilting F, Ortega Cortés J, Bernal A, Palanco S et al. (2024) Baseprod: The bardenas semi-desert planetary rover dataset. *Scientific Data* 11(1): 1054.
- Giubilato R, Stürzl W, Wedler A and Triebel R (2022) Challenges of slam in extremely unstructured environments: The dlr planetary stereo, solid-state lidar, inertial dataset. *IEEE Robotics and Automation Letters* 7(4): 8721–8728.
- Gramuglia F, Ripiccini E, Fenoglio CA, Wu ML, Paolozzi L, Bruschini C and Charbon E (2022) Sub-10 ps minimum ionizing particle detection with geiger-mode APDs. *Frontiers in Physics* 10. DOI:https://doi.org/10.3389/fphy.2022.849237.
- Hansen M, Wong U and Fong T (2024) The POLAR Traverse dataset: A dataset of stereo camera images simulating traverses across lunar polar terrain under extreme lighting conditions. *NASA Ames Research Center*.
- Kleinhenz J, Quinn J, Colaprete A, Captain J, Ennico-Smith K, Lim D, Aguilar-Ayala R, Hancock M, Zacny K, Chu P et al. (2024) Lunar surface missions for resource reconnaissance: NASA's PRIME-1 and VIPER. In: *Space Resources Round Table*.
- Labbe M and Michaud F (2019) RTAB-Map as an open-source lidar and visual simultaneous localization and mapping library for large-scale and long-term online operation. *Journal of Field Robotics* 36(2): 416.
- Lowe DG (2004) Distinctive image features from scale-invariant keypoints. *International journal of computer vision* 60: 91–110.
- Ludvig P, Calzada-Diaz A, Olivares Mendez MA, Voos H and Lamamy J (2020) Building a piece of the moon: Construction of two indoor lunar analogue environments. In: *71st International Astronautical Congress (IAC)–The CyberSpace Edition*.
- Michalet X, Ulku A, Smith JT, Bruschini C, Weiss S, Charbon E and Intes X (2022) NIR Fluorescence lifetime macroscopic imaging with a time-gated SPAD camera. In: *Multiphoton Microscopy in the Biomedical Sciences XXII*, volume 11965. SPIE, pp. 29–37.
- Morimoto K, Ardelean A, Wu ML, Ulku AC, Antolovic IM, Bruschini C and Charbon E (2020) Megapixel time-gated SPAD image sensor for 2D and 3D imaging applications. *Optica* 7(4): 346–354.
- Padma T (2023) India's Moon mission: Four things Chandrayaan-3 has taught scientists. *Nature* 621(7979): 456–456.
- Pessia R, Ishigami G and Jodelet Q (2019) Artificial lunar landscape dataset. DOI:10.34740/kaggle/dsv/489236. URL <https://www.kaggle.com/dsv/489236>.
- Richard A, Kamohara J, Uno K, Santra S, van der Meer D, Olivares-Mendez M and Yoshida K (2024) OmniLRS: A photorealistic simulator for lunar robotics. In: *IEEE International Conference on Robotics and Automation (ICRA)*. IEEE, pp. 16901–16907.
- Rodríguez-Martínez D, Van Winnendael M and Yoshida K (2019) High-speed mobility on planetary surfaces: A technical review. *Journal of Field Robotics* 36(8): 1436–1455.
- Ruble E, Rabaud V, Konolige K and Bradski G (2011) ORB: An efficient alternative to SIFT or SURF. In: *2011 International conference on computer vision*. IEEE, pp. 2564–2571.
- Song J, Richard A and Olivares-Mendez M (2024) Joint spatial-temporal calibration for camera and global pose sensor. In: *2024 International Conference on 3D Vision (3DV)*. IEEE, pp. 1027–1036.
- Vayugundla M, Steidle F, Smisek M, Schuster MJ, Bussmann K and Wedler A (2018) Datasets of long range navigation experiments in a moon analogue environment on mount etna. In: *ISR 2018; 50th International Symposium on Robotics*. pp. 1–7.
- Wang C, Jia Y, Xue C, Lin Y, Liu J, Fu X, Xu L, Huang Y, Zhao Y, Xu Y et al. (2024a) Scientific objectives and payload configuration of the Chang'E-7 mission. *National Science Review* 11(2): nwad329.
- Wang Y, Yuan T, Liu C, Wu Q and Qian J (2024b) the real chang'e lunar landscape dataset. DOI:10.21227/9y8q-dx27. URL <https://dx.doi.org/10.21227/9y8q-dx27>.
- Wong U, Nefian A, Edwards L, Buoyssounouse X, Furlong PM, Deans M and Fong T (2017) Polar Optical Lunar Analog Reconstruction (POLAR) Stereo Dataset. *NASA Ames Research Center*.
- Zhang Y, Liu B, Di K, Liu S, Yue Z, Han S, Wang J, Wan W and Xie B (2023) Analysis of illumination conditions in the Lunar South Polar Region using multi-temporal high-resolution orbital images. *Remote Sensing* 15(24): 5691.
- Zhao J, Lyons A, Ulku A, Defienne H, Faccio D and Charbon E (2022) Light detection and ranging with entangled photons. *Optics Express* 30(3): 3675–3683. DOI:https://doi.org/10.1098/rsta.2013.0100.

Funding

This work was supported in part by armasuisse Science and Technology (contract number 8003538860) under the project “Monocular SPAD camera for enhanced vision in complex and uncertain environments.”